Geophysical Journal International

Geophys. J. Int. (2012) **188,** 177–194 doi: 10.1111/j.1365-246X.2011.05240.x

SH-wave scattering by a semi-elliptical hill using a null-field boundary integral equation method and a hybrid method

Jeng-Tzong Chen,[1,2] Jia-Wei Lee[1] and Wen-Shinn Shyu[3]

[1] *Department of Harbor and River Engineering, National Taiwan Ocean University, Keelung, Taiwan. E-mail: jtchen@mail.ntou.edu.tw*
[2] *Department of Mechanical and Mechatronic Engineering, National Taiwan Ocean University, Keelung, Taiwan*
[3] *Department of Civil Engineering, National Pingtung University of Science and Technology, Pingtung, Taiwan*

Accepted 2011 September 21. Received 2011 August 27; in original form 2011 February 16

SUMMARY

Following the success of seismic analysis of a semi-circular hill, the problem of *SH*-wave scattering by a semi-elliptical hill is revisited by using the null-field boundary integral equation method (BIEM). To fully use the analytical property in the null-field boundary integral equation approach in conjunction with degenerate kernels for solving the semi-elliptical hill scattering problem, the problem is decomposed to two regions to produce elliptical boundaries by using the technique of taking free body. One is the half-plane problem containing a semi-elliptical boundary. This semi-infinite problem is imbedded in an infinite plane with an artificial elliptical boundary such that degenerate kernel can be fully applied. The other is an interior problem bounded by an elliptical boundary. The degenerate kernel in the elliptic coordinates for two subdomains is used to expand the closed-form fundamental solution. The semi-analytical formulation in companion with matching boundary conditions yields six constraint equations. Instead of finding admissible wave-expansion bases, our null-field BIEM in conjunction with degenerate kernels has the five features over the conventional BIEM/BEM, (1) free of calculating principal values, (2) exponential convergence, (3) elimination of boundary-layer effect, (4) meshless and (5) well-posed system. All numerical results are compared well with those of using the hybrid method which is also described in this paper. It is interesting to find that a focusing phenomenon is also observed in this study.

Key words: Earthquake ground motions; Earthquake interaction, forecasting, and prediction; Wave scattering and diffraction.

1 INTRODUCTION

Taiwan locates in the Pacific Ring of Fire, which is an area with a large number of earthquakes and volcanic eruptions. It results in significant displacement amplitude on the canyon, hill and ground surface because of scattering and diffraction of seismic waves. Studying the vibrational response of the soil because of earthquakes is an important issue in this area. Based on assumptions of linear elastic, isotropic and homogenous medium for the soil, problems of *SH*-wave scattering can be formulated to the 2-D Helmholtz equation.

Regarding *SH*-wave scattering problems by the alluvial valley and canyon, Trifunac derived analytical solutions for semi-circular cases with alluvial and without alluvial in 1971 (Trifunac 1971, 1973)), respectively. Later, Yuan & Liao (1994) employed the approach of wavefunction expansion to deal with problems of *SH*-waves scattered by a cylindrical canyon of circular-arc cross-section. Wong and Trifunac extended a circular case to a semi-elliptical canyon (Wong & Trifunac 1974a) and alluvial (Wong & Trifunac 1974b). Later, Wong (1982) extended *SH* wave to the *P*, *SV* and Rayleigh waves. For the multilayers problems, Vogt *et al*. (1988) have employed the indirect boundary element method (BEM) to solve the canyon problem of arbitrary shape in a layered half-space. The reflection waves caused by a hill are more complex than a canyon from the point of wave physics. Mathematically speaking, hill scattering is not easier than the canyon case not only because of its convex geometry but also its solution space. It means that the closed-form or analytical solution is not easy to derive. Therefore, numerical methods are required.

Although Sánchez-Sesma & Campillo (1991) have solved the semi-elliptical hill problem, only *P*, *SV* and Rayleigh waves were considered. The literature for the semi-elliptical hill subject to *SH* wave is very limited. To authors' best knowledge, only one paper (Cao *et al*. 2001) on this topic was found.

Numerical methods were used to solve this kind of problems including the wave-expansion method (Yuan & Men 1992; Yuan & Liao 1996; Tsaur & Chang 2009), BIEM/BEM (Chen *et al*. 2008a, 2011b), hybrid method (Mei 1980) and spectral element method (SEM;

Komatitsch *et al*. 2004). For the BEM, direct (Álvarez-Rubio *et al*. 2004; Kawakami & Mogi 2007) and indirect formulations (Sánchez-Sesma *et al*. 2001) have been employed. Regarding the fundamental solution, Kawase (1988) used the discrete wavenumber Green's function in BEM. For the conventional BEM, the closed-form fundamental solution is used. On the other hand, Chen *et al.* (2008a, 2011b) employed the degenerate kernel for the fundamental solution and proposed the null-field integral equation approach. To consider the complex shape of canyon or hill, the hybrid method and SEM are flexible to solve this problem. The main care for the wave-expansion method is the selection of completeness of the wavefunction base. As quoted by Tsaur & Chang (2009) 'Unfortunately, their series solution for such a problem is in error because of unsuitable connection between the domain decomposition and the expression of corresponding wavefield.', this pointed out that finding admissible bases is important. This is the reason why Lee *et al*. (2006) improved the analytical wave series solution of Yuan and his coworkers' papers (Yuan & Men 1992; Yuan & Liao 1996) to take care of the stress singularity on the rim of the hill. A convenient criterion of completeness was mentioned by Sánchez-Sesma *et al*. (1982). The expansion can converge uniformly if the Rayleigh hypothesis is satisfied.

In 2008, Chen *et al*. (2008a) employed the null-field BIEM to solve *SH*-wave scattering problems by multiple semi-circular alluvial valleys. Because of the circular geometry, Chen and his coworkers naturally employed the null-field BIEM in conjunction with degenerate kernels and Fourier series. Therefore, their proposed approach is a semi-analytical approach. The expansion of closed-form fundamental solution is also one kind of addition theorem, which has been widely used in the approach of wavefunction expansion. The theoretical point of degenerate kernel is that the two-point function for the fundamental solution is separated to source and field point. Although only boundary elements along the free surface are needed in the conventional BEM, it is required to compute singular or hypersingular integrals in the principal value sense by using the bump contour approach. Owing to introduce the degenerate kernels instead of closed-form kernel functions, it is free for calculating principal values in the null-field BIEM. Besides, five merits over the conventional BIEM/BEM, (1) free of calculating principal values, (2) exponential convergence, (3) elimination of boundary-layer effect, (4) meshless and (5) well-posed system, were demonstrated. A large amount of work to demonstrate the five advantages have been done by Chen and his coworkers for Laplace (Chen & Wu 2007), Helmholtz (Chen *et al*. 2007), biharmonic (Chen *et al*. 2008b) and biHelmholtz (Lee & Chen 2010b) problems. The key ingredient of null-field BIEM is the degenerate kernel, which is of theoretical use in the development of integral operator. Although degenerate kernel is not popular to engineers as well as mathematicians, the degenerate kernel method is conceptually simple and efficient (Atkinson 1997). After using degenerate kernel instead of fundamental solution, boundary contour integration can be easily implemented. Therefore, BIEM is nothing more than linear algebra (Cochran 1982). The efficiency is promoted in three aspects, analytical boundary integral without numerical error, natural bases for boundary densities and exact description of boundary geometry. Based on the same idea, the null-field BIEM was also applied to solve problems containing elliptical boundaries (Chen *et al*. 2010). Degenerate kernels using the Bessel function in the circular case are changed to Mathieu function for the elliptical boundary. Mathematically speaking, degenerate kernel is a finite-rank approximation of the closed-form fundamental solution. Successful applications to vibration (Chen *et al*. 2011a) and water wave problems (Lee & Chen 2010a; Chen & Lee 2011) have also been done.

No matter what the approach is used, a benchmark example to demonstrate the validity of numerical approaches is required. For the hill scattering case, four popular examples, semi-circular hill (Yuan & Men 1992; Chen *et al*. 2011b), semi-elliptical hill (Cao *et al*. 2001), Gaussian hill (Fu 2005) and half-sine hill (Kamalian *et al*. 2008), have been widely used. For clarity, a semi-elliptical hill is our focus by testing our formulation. To deal with this problem, the idea of domain decomposition was used in earthquake, ocean and electrical engineering. It is interesting to find that earthquake engineers always cut the circular arc to have a circular region as the second domain (Yuan & Men 1992) in Fig. 1(a). In harbour resonance (Lee 1971) and electromagnetics (Wood & Wood 1999), a straight line was introduced to separate into two regions in Fig. 1(b).

Focusing effect in optics, acoustics and electromagnetics has been noted but only a little in elastic wave has been studied even though the Northridge earthquake damage was examined to be caused by geologic focusing of seismic wave (USGS & SCEC 1994; Davis *et al*. 2000). Tsaur & Chang (2009) employed the wavefunction expansion approach to find the focusing behaviour for the shallow circular arc hill in both time and frequency domains. For the semi-circular hill, focusing phenomenon was also observed by Chen *et al*. (2011b). The maximum response may occur beneath the hill boundary, which may cause failure for underground structures. In this paper, we may wonder whether it also happens or not for the semi-elliptical hill.

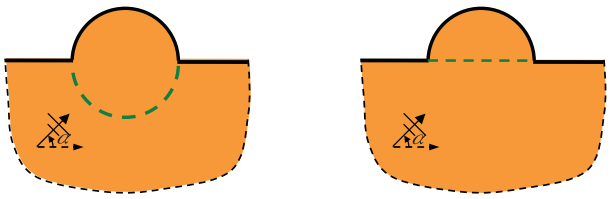

Figure 1. Problem sketch of scattering problem with semi-circular topography: (a) seismic analysis for a hill scattering and (b) harbour resonance and electromagnetics.

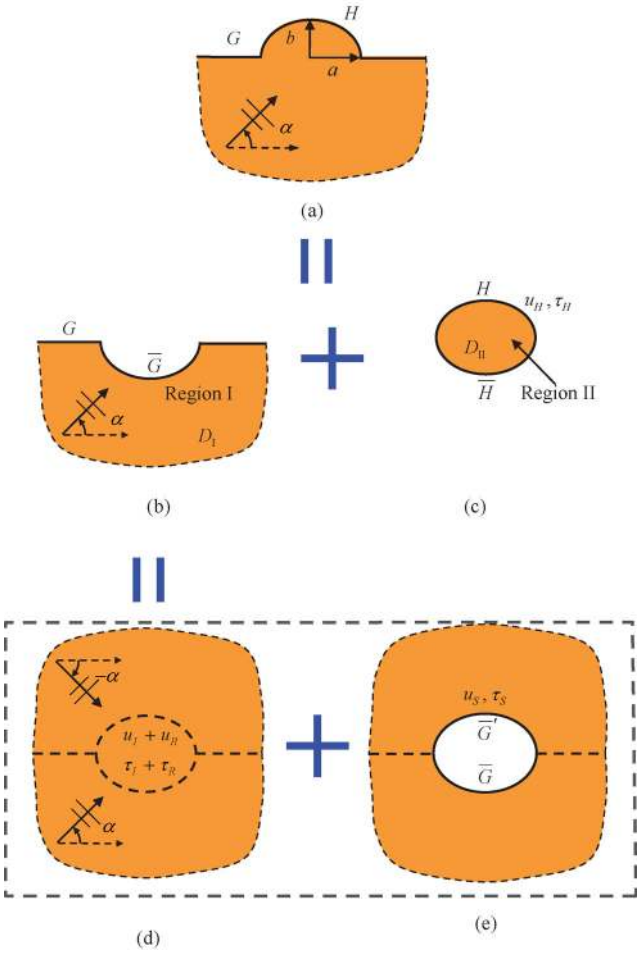

Figure 2. Decomposition of the semi-elliptical hill scattering problem. (a) Original problem, (b) a half-plane subject to traction free B.C. along the horizontal ground surface, (c) an elliptical region, (d) an infinite plane and (e) an infinite plane containing an elliptical hole.

Accordingly, we aim to extend the approach to deal with *SH*-wave scattering problems by a semi-elliptical hill. Instead of finding admissible wave-expansion bases, we construct six constraint equations from the null-field BIEM formulations and matching boundary conditions. Numerical results will be compared with those of using the hybrid method. Focusing phenomenon will be examined.

2 PROBLEM STATEMENT

A scattering problem subject to a *SH*-wave impinging on a semi-elliptical hill is shown in Fig. 2(a). The material property of the soil is assumed to be linear elastic, isotropic and homogenous. Therefore, the governing equation of the antiplane motion is the 2-D Helmholtz equation as follows:

$$(\nabla^2 + k^2)u(\mathbf{x}) = 0, \quad \mathbf{x} \in D, \tag{1}$$

where ∇^2 is the Laplacian operator, k is the shear wavenumber, $u(\mathbf{x})$ is the antiplane displacement of the semi-elliptical hill, $\mathbf{x}$ is the field point and D is the domain of interest. The two components of the field point $\mathbf{x}$ in terms of the Cartesian and elliptical coordinates are (x, y) and $(\xi_{\mathbf{x}}, \eta_{\mathbf{x}})$, respectively. The boundary condition is the traction-free boundary condition as shown below

$$\tau(\mathbf{x}) = \mu t(\mathbf{x}) = \mu \frac{\partial u(\mathbf{x})}{\partial n_{\mathbf{x}}} = 0, \ \mathbf{x} \in B, \tag{2}$$

where $\tau(\mathbf{x})$ is the traction along the horizontal ground surface and the hill border, $t(\mathbf{x})$ is the normal derivative of $u(\mathbf{x})$, μ is the shear modulus, $n_{\mathbf{x}}$ denotes the unit outward normal vector at the field point and B is the boundary.

The incident plane *SH* wave $[u_I(\mathbf{x})]$ is expressed as

$$u_I(\mathbf{x}) = A_0 e^{ik[x\cos(\alpha)+y\sin(\alpha)]}, \tag{3}$$

where A_0 is the amplitude of the *SH* wave and α is the incident angle.

3 DUAL BOUNDARY INTEGRAL FORMULATIONS AND DEGENERATE KERNELS

By introducing degenerate kernels, the collocation point can be located on the real boundary without need of calculating principal value in the bump contour approach. By choosing the proper degenerate kernels, the representations of the conventional integral equations including the boundary point can be written as

$$2\pi u(\mathbf{x}) = \int_B T(\mathbf{s},\mathbf{x})u(\mathbf{s})\mathrm{d}B(\mathbf{s}) - \int_B U(\mathbf{s},\mathbf{x})t(\mathbf{s})\mathrm{d}B(\mathbf{s}), \quad \mathbf{x} \in D \cup B, \tag{4}$$

$$2\pi t(\mathbf{x}) = \int_B M(\mathbf{s},\mathbf{x})u(\mathbf{s})\mathrm{d}B(\mathbf{s}) - \int_B L(\mathbf{s},\mathbf{x})t(\mathbf{s})\mathrm{d}B(\mathbf{s}), \quad \mathbf{x} \in D \cup B \tag{5}$$

and

$$0 = \int_B T(\mathbf{s},\mathbf{x})u(\mathbf{s})\mathrm{d}B(\mathbf{s}) - \int_B U(\mathbf{s},\mathbf{x})t(\mathbf{s})\mathrm{d}B(\mathbf{s}), \quad \mathbf{x} \in D^c \cup B, \tag{6}$$

$$0 = \int_B M(\mathbf{s},\mathbf{x})u(\mathbf{s})\mathrm{d}B(\mathbf{s}) - \int_B L(\mathbf{s},\mathbf{x})t(\mathbf{s})\mathrm{d}B(\mathbf{s}), \quad \mathbf{x} \in D^c \cup B, \tag{7}$$

where $\mathbf{s}$ is the source point, D^c is the complementary domain and the kernel function $U(\mathbf{s},\mathbf{x})$ is the fundamental solution which satisfies

$$(\nabla^2 + k^2)U(\mathbf{s},\mathbf{x}) = 2\pi\delta(\mathbf{x}-\mathbf{s}), \tag{8}$$

in which $\delta(\mathbf{x}-\mathbf{s})$ denotes the Dirac-delta function. It is noted that the four kernels in eqs (4)–(7) should be chosen for corresponding degenerate kernels. The other kernel functions, $T(\mathbf{s},\mathbf{x})$, $L(\mathbf{s},\mathbf{x})$ and $M(\mathbf{s},\mathbf{x})$, are defined by

$$T(\mathbf{s},\mathbf{x}) = \frac{\partial U(\mathbf{s},\mathbf{x})}{\partial n_{\mathbf{s}}}, \tag{9}$$

$$L(\mathbf{s},\mathbf{x}) = \frac{\partial U(\mathbf{s},\mathbf{x})}{\partial n_{\mathbf{x}}}, \tag{10}$$

$$M(\mathbf{s},\mathbf{x}) = \frac{\partial^2 U(\mathbf{s},\mathbf{x})}{\partial n_{\mathbf{s}}\partial n_{\mathbf{x}}}, \tag{11}$$

where $n_{\mathbf{s}}$ denotes the unit outward normal vector at the source point. It is noted that eqs (4)–(7) can contain the boundary point ($\mathbf{x} \to B$) because the kernel functions (U, T, L and M) are expressed in terms of proper degenerate kernels which will be elaborated on later in eq. (17)–(20).

The closed-form fundamental solution as previously mentioned is:

$$U(\mathbf{s},\mathbf{x}) = -\frac{i\pi H_0^{(1)}(kr)}{2}, \tag{12}$$

where $r \equiv |\mathbf{s}-\mathbf{x}|$ is the distance between the source point and the field point and $H_0^{(1)}$ is the zeroth-order Hankel function of the first kind. Based on the property of separation variables in the elliptical coordinates, the closed-form fundamental solution $U(\mathbf{s},\mathbf{x})$ of eq. (12), other kernel functions $T(\mathbf{s},\mathbf{x})$, $L(\mathbf{s},\mathbf{x})$ and $M(\mathbf{s},\mathbf{x})$ can be expressed as

$$U(\mathbf{s},\mathbf{x}) = \begin{cases} U^E(\mathbf{s},\mathbf{x}) = \lim\limits_{N\to\infty} U_N^E(\mathbf{s},\mathbf{x}), & \xi_{\mathbf{x}} \geq \xi_{\mathbf{s}}, \\ U^I(\mathbf{s},\mathbf{x}) = \lim\limits_{N\to\infty} U_N^I(\mathbf{s},\mathbf{x}), & \xi_{\mathbf{x}} < \xi_{\mathbf{s}}, \end{cases} \tag{13}$$

$$T(\mathbf{s},\mathbf{x}) = \begin{cases} T^E(\mathbf{s},\mathbf{x}) = \lim\limits_{N\to\infty} T_N^E(\mathbf{s},\mathbf{x}), & \xi_{\mathbf{x}} > \xi_{\mathbf{s}}, \\ T^I(\mathbf{s},\mathbf{x}) = \lim\limits_{N\to\infty} T_N^I(\mathbf{s},\mathbf{x}), & \xi_{\mathbf{x}} < \xi_{\mathbf{s}}, \end{cases} \tag{14}$$

$$L(\mathbf{s},\mathbf{x}) = \begin{cases} L^E(\mathbf{s},\mathbf{x}) = \lim\limits_{N\to\infty} L_N^E(\mathbf{s},\mathbf{x}), & \xi_{\mathbf{x}} > \xi_{\mathbf{s}}, \\ L^I(\mathbf{s},\mathbf{x}) = \lim\limits_{N\to\infty} L_N^I(\mathbf{s},\mathbf{x}), & \xi_{\mathbf{x}} < \xi_{\mathbf{s}}, \end{cases} \tag{15}$$

$$M(\mathbf{s},\mathbf{x}) = \begin{cases} M^E(\mathbf{s},\mathbf{x}) = \lim\limits_{N\to\infty} M_N^E(\mathbf{s},\mathbf{x}), & \xi_{\mathbf{x}} \geq \xi_{\mathbf{s}}, \\ M^I(\mathbf{s},\mathbf{x}) = \lim\limits_{N\to\infty} M_N^I(\mathbf{s},\mathbf{x}), & \xi_{\mathbf{x}} < \xi_{\mathbf{s}}, \end{cases} \tag{16}$$

where $U_N^E(\mathbf{s},\mathbf{x})$, $U_N^I(\mathbf{s},\mathbf{x})$, $T_N^E(\mathbf{s},\mathbf{x})$, $T_N^I(\mathbf{s},\mathbf{x})$, $L_N^E(\mathbf{s},\mathbf{x})$, $L_N^I(\mathbf{s},\mathbf{x})$, $M_N^E(\mathbf{s},\mathbf{x})$ and $M_N^I(\mathbf{s},\mathbf{x})$ are degenerate kernels (finite-rank approximation; Morse & Feshbach 1953) as shown below

$$\begin{cases} U_N^E(\mathbf{s},\mathbf{x}) = -2\pi i \left(\sum_{m=0}^{N} \left[\dfrac{Se_m(q,\eta_\mathbf{s})}{M_m^e(q)} \right] Se_m(q,\eta_\mathbf{x}) Je_m(q,\xi_\mathbf{s}) He_m(q,\xi_\mathbf{x}) \right. \\ \qquad \left. + \sum_{m=1}^{N} \left[\dfrac{So_m(q,\eta_\mathbf{s})}{M_m^o(q)} \right] So_m(q,\eta_\mathbf{x}) Jo_m(q,\xi_\mathbf{s}) Ho_m(q,\xi_\mathbf{x}) \right), \quad \xi_\mathbf{x} \geq \xi_\mathbf{s}, \\ U_N^I(\mathbf{s},\mathbf{x}) = -2\pi i \left(\sum_{m=0}^{N} \left[\dfrac{Se_m(q,\eta_\mathbf{s})}{M_m^e(q)} \right] Se_m(q,\eta_\mathbf{x}) Je_m(q,\xi_\mathbf{x}) He_m(q,\xi_\mathbf{s}) \right. \\ \qquad \left. + \sum_{m=1}^{N} \left[\dfrac{So_m(q,\eta_\mathbf{s})}{M_m^o(q)} \right] So_m(q,\eta_\mathbf{x}) Jo_m(q,\xi_\mathbf{x}) Ho_m(q,\xi_\mathbf{s}) \right), \quad \xi_\mathbf{x} < \xi_\mathbf{s}, \end{cases} \tag{17}$$

$$\begin{cases} T_N^E(\mathbf{s},\mathbf{x}) = -2\pi i \dfrac{1}{J_\mathbf{s}} \left(\sum_{m=0}^{N} \left[\dfrac{Se_m(q,\eta_\mathbf{s})}{M_m^e(q)} \right] Se_m(q,\eta_\mathbf{x}) Je'_m(q,\xi_\mathbf{s}) He_m(q,\xi_\mathbf{x}) \right. \\ \qquad \left. + \sum_{m=1}^{N} \left[\dfrac{So_m(q,\eta_\mathbf{s})}{M_m^o(q)} \right] So_m(q,\eta_\mathbf{x}) Jo'_m(q,\xi_\mathbf{s}) Ho_m(q,\xi_\mathbf{x}) \right), \quad \xi_\mathbf{x} > \xi_\mathbf{s}, \\ T_N^I(\mathbf{s},\mathbf{x}) = -2\pi i \dfrac{1}{J_\mathbf{s}} \left(\sum_{m=0}^{N} \left[\dfrac{Se_m(q,\eta_\mathbf{s})}{M_m^e(q)} \right] Se_m(q,\eta_\mathbf{x}) Je_m(q,\xi_\mathbf{x}) He'_m(q,\xi_\mathbf{s}) \right. \\ \qquad \left. + \sum_{m=1}^{N} \left[\dfrac{So_m(q,\eta_\mathbf{s})}{M_m^o(q)} \right] So_m(q,\eta_\mathbf{x}) Jo_m(q,\xi_\mathbf{x}) Ho'_m(q,\xi_\mathbf{s}) \right), \quad \xi_\mathbf{x} < \xi_\mathbf{s}, \end{cases} \tag{18}$$

$$\begin{cases} L_N^E(\mathbf{s},\mathbf{x}) = -2\pi i \dfrac{1}{J_\mathbf{x}} \left(\sum_{m=0}^{N} \left[\dfrac{Se_m(q,\eta_\mathbf{s})}{M_m^e(q)} \right] Se_m(q,\eta_\mathbf{x}) Je_m(q,\xi_\mathbf{s}) He'_m(q,\xi_\mathbf{x}) \right. \\ \qquad \left. + \sum_{m=1}^{N} \left[\dfrac{So_m(q,\eta_\mathbf{s})}{M_m^o(q)} \right] So_m(q,\eta_\mathbf{x}) Jo_m(q,\xi_\mathbf{s}) Ho'_m(q,\xi_\mathbf{x}) \right), \quad \xi_\mathbf{x} > \xi_\mathbf{s}, \\ L_N^I(\mathbf{s},\mathbf{x}) = -2\pi i \dfrac{1}{J_\mathbf{x}} \left(\sum_{m=0}^{N} \left[\dfrac{Se_m(q,\eta_\mathbf{s})}{M_m^e(q)} \right] Se_m(q,\eta_\mathbf{x}) Je'_m(q,\xi_\mathbf{x}) He_m(q,\xi_\mathbf{s}) \right. \\ \qquad \left. + \sum_{m=1}^{N} \left[\dfrac{So_m(q,\eta_\mathbf{s})}{M_m^o(q)} \right] So_m(q,\eta_\mathbf{x}) Jo'_m(q,\xi_\mathbf{x}) Ho_m(q,\xi_\mathbf{s}) \right), \quad \xi_\mathbf{x} < \xi_\mathbf{s}, \end{cases} \tag{19}$$

$$\begin{cases} M_N^E(\mathbf{s},\mathbf{x}) = -2\pi i \dfrac{1}{J_\mathbf{s} J_\mathbf{x}} \left(\sum_{m=0}^{N} \left[\dfrac{Se_m(q,\eta_\mathbf{s})}{M_m^e(q)} \right] Se_m(q,\eta_\mathbf{x}) Je'_m(q,\xi_\mathbf{s}) He'_m(q,\xi_\mathbf{x}) \right. \\ \qquad \left. + \sum_{m=1}^{N} \left[\dfrac{So_m(q,\eta_\mathbf{s})}{M_m^o(q)} \right] So_m(q,\eta_\mathbf{x}) Jo'_m(q,\xi_\mathbf{s}) Ho'_m(q,\xi_\mathbf{x}) \right), \quad \xi_\mathbf{x} \geq \xi_\mathbf{s}, \\ M_N^I(\mathbf{s},\mathbf{x}) = -2\pi i \dfrac{1}{J_\mathbf{s} J_\mathbf{x}} \left(\sum_{m=0}^{N} \left[\dfrac{Se_m(q,\eta_\mathbf{s})}{M_m^e(q)} \right] Se_m(q,\eta_\mathbf{x}) Je'_m(q,\xi_\mathbf{x}) He'_m(q,\xi_\mathbf{s}) \right. \\ \qquad \left. + \sum_{m=1}^{N} \left[\dfrac{So_m(q,\eta_\mathbf{s})}{M_m^o(q)} \right] So_m(q,\eta_\mathbf{x}) Jo'_m(q,\xi_\mathbf{x}) Ho'_m(q,\xi_\mathbf{s}) \right), \quad \xi_\mathbf{x} < \xi_\mathbf{s}, \end{cases} \tag{20}$$

in which $(\xi_\mathbf{s},\ \eta_\mathbf{s})$ are the elliptical coordinates of the source point $\mathbf{s}$, q is defined by

$$q = \left(ck/2\right)^2, \tag{21}$$

where c is the half distance between the two foci of the ellipse. Special functions, Se_m and So_m, are the mth-order even and odd Mathieu functions (angular), respectively; Je_m and Jo_m are the mth-order even and odd modified Mathieu functions (radial) of the first kind, respectively; He_m and Ho_m are the even and odd mth-order modified Mathieu functions (Mathieu–Hankel functions) of the third kind,

respectively and are defined as (Abramowitz & Stegun 1965; Zhang & Jin 1996)

$$He_m(q,\xi) = Je_m(q,\xi) + iYe_m(q,\xi), \tag{22}$$

$$Ho_m(q,\ \xi) = Jo_m(q,\xi) + iYo_m(q,\xi), \tag{23}$$

in which Ye_m and Yo_m are the mth-order even and odd the modified Mathieu functions of the second kind, respectively. $J_{\mathbf{x}}$ and $J_{\mathbf{s}}$ are the Jacobian term for the field point $\mathbf{x}$ and source point $\mathbf{s}$, respectively as shown below

$$J_{\mathbf{x}} = c\sqrt{[\sinh(\xi_{\mathbf{x}})\cos(\eta_{\mathbf{x}})]^2 + [\cosh(\xi_{\mathbf{x}})\sin(\eta_{\mathbf{x}})]^2}, \tag{24}$$

$$J_{\mathbf{s}} = c\sqrt{[\sinh(\xi_{\mathbf{s}})\cos(\eta_{\mathbf{s}})]^2 + [\cosh(\xi_{\mathbf{s}})\sin(\eta_{\mathbf{s}})]^2}. \tag{25}$$

The normalized constants M_m^e and M_m^o can be obtained by

$$M_m^e(q) = \int_0^{2\pi} [Se_m(q,\eta)]^2 \mathrm{d}\eta = \pi, \tag{26}$$

$$M_m^o(q) = \int_0^{2\pi} [So_m(q,\eta)]^2 \mathrm{d}\eta = \pi. \tag{27}$$

4 DECOMPOSITION OF THE PROBLEM AND SIX CONSTRAINTS

4.1 Decomposition of the problem

To fully use the semi-analytical property of the null-field BIEM for solving boundary value problems containing elliptical boundaries, the original problem of a semi-elliptical hill is divided into two regions as shown in Fig. 2, where G and H denote the horizontal ground surface and semi-elliptical hill border, respectively. A half-plane region (Region I) is shown in Fig. 2(b) and the other is an enclosed region bounded by the elliptical boundary (Region II) as shown in Fig. 2(c). In Fig. 2(b), a half-plane problem with an artificial boundary ($\overline{G}$ or $\overline{H}$) can be imbedded to an infinite domain. Then, it can be decomposed to an infinite plane with incident and reflective waves and an infinite plane containing an elliptical hole which satisfies the specified boundary condition as shown in Figs 2(d) and (e), respectively.

4.2 Expansion of boundary density

To fully use the geometry of elliptical boundary, the boundary displacement $u(\mathbf{s})$ and traction $\tau(\mathbf{s})$ along the elliptical boundary can be approximated by employing the eigenfunction expansion. Therefore, we obtain

$$u_S(\mathbf{s}) = \sum_{n=0}^{\infty} a_n^S Se_n(q,\eta_{\mathbf{s}}) + \sum_{n=1}^{\infty} b_n^S So_n(q,\eta_{\mathbf{s}}), \tag{28}$$

$$\tau_S(\mathbf{s}) = \mu t_S(\mathbf{s}) = \mu \frac{1}{J_{\mathbf{s}}} \left(\sum_{n=0}^{\infty} p_n^S Se_n(q,\eta_{\mathbf{s}}) + \sum_{n=1}^{\infty} q_n^S So_n(q,\eta_{\mathbf{s}}) \right), \tag{29}$$

$$u_H(\mathbf{s}) = \sum_{n=0}^{\infty} a_n^H Se_n(q,\eta_{\mathbf{s}}) + \sum_{n=1}^{\infty} b_n^H So_n(q,\eta_{\mathbf{s}}), \tag{30}$$

$$\tau_H(\mathbf{s}) = \mu t_H(\mathbf{s}) = \mu \frac{1}{J_{\mathbf{s}}} \left(\sum_{n=0}^{\infty} p_n^H Se_n(q,\eta_{\mathbf{s}}) + \sum_{n=1}^{\infty} q_n^H So_n(q,\eta_{\mathbf{s}}) \right), \tag{31}$$

where a_n^S, b_n^S, p_n^S, q_n^S, a_n^H, b_n^H p_n^H and q_n^H are the unknown coefficients of the eigenfunctions, the superscripts 'S' and 'H' denote the region I in Fig. 2(c) and the region II in Fig. 2(e), respectively. The Jacobian term $J_{\mathbf{s}}$ may appear either in the kernel functions of eqs (18)–(20), the boundary densities of eqs (29) and (31) or the elliptical boundary contour integration ($\mathrm{d}B(\mathbf{s}) = J_{\mathbf{s}}\mathrm{d}\eta_{\mathbf{s}}$). We may worry about the possible use of orthogonal relations for the Mathieu bases because of the presence of $J_{\mathbf{s}}$. Fortunately, the Jacobian terms can be cancelled each other out by artificially introducing a Jacobian term in the expansion of boundary flux. Therefore, the orthogonal relations can be fully used in the contour integration of an elliptical boundary and they can be analytically determined. In the real computation, only finite $(2M+1)$ terms are truncated in the summation of eqs (28)–(31).

4.3 Formulations for each subdomain and matching of boundary conditions

To formulate the original problem after decomposition, six equations are obtained from BIEs and match of BCs as shown later.

4.3.1 Exterior problem by using the null-field BIEM

For the exterior problem containing an elliptical hole subject to the specified boundary condition as shown in Fig. 2(e), the null-field BIEM for the boundary point in eq. (6) yields

$$\int \left[T^I(\mathbf{s},\mathbf{x})u_S(\mathbf{s}) - U^I(\mathbf{s},\mathbf{x})t_S(\mathbf{s})\right] \mathrm{d}B(\mathbf{s}) = 0,\ \mathbf{x} \in \overline{G} \cup \overline{G}', \tag{32}$$

where $\overline{G}$ and $\overline{G}'$ are the upper- and lower-half parts of the artificial elliptical boundary in Fig. 2(e), respectively.

4.3.2 Interior problem by using the null-field BIEM

For the null-field BIEM of the elliptical domain in Fig. 2(c), we have the null-field BIEM for the boundary point of the region II

$$\int \left[T^E(\mathbf{s},\mathbf{x})u_H(\mathbf{s}) - U^E(\mathbf{s},\mathbf{x})t_H(\mathbf{s})\right] \mathrm{d}B(\mathbf{s}) = 0,\ \mathbf{x} \in H \cup \overline{H}, \tag{33}$$

where H and $\overline{H}$ are the upper- and lower-half parts of the elliptical boundary in Fig. 2(c), respectively.

4.3.3 Continuity condition on the artificial interface

The continuity condition of the displacement on the artificial interface, we have

$$u_I(\mathbf{x}) + u_R(\mathbf{x}) + u_S(\mathbf{x}) = u_H(\mathbf{x}),\ \pi \le \eta_{\mathbf{x}} \le 2\pi, \tag{34}$$

where $\mathbf{x} = (\xi_{\mathbf{x}}, \eta_{\mathbf{x}})$ and $u_R(\mathbf{x})$ is the reflection wavefield as shown below

$$u_R(\mathbf{x}) = A_0 e^{ik[x\cos(-\alpha)+y\sin(-\alpha)]}. \tag{35}$$

4.3.4 Equilibrium condition on the artificial interface

The equilibrium condition of force on the artificial interface, we have

$$-[\tau_I(\mathbf{x}) + \tau_R(\mathbf{x}) + \tau_S(\mathbf{x})] = \tau_H(\mathbf{x}),\ \pi \le \eta_{\mathbf{x}} \le 2\pi. \tag{36}$$

4.3.5 Boundary condition on the hill border

The hill border boundary (H) is subject to the traction-free boundary condition (Neumann type) as shown below:

$$\tau_H(\mathbf{x}) = 0,\ 0 \le \eta_{\mathbf{x}} \le \pi. \tag{37}$$

4.3.6 Boundary condition on the horizontal ground surface

The half-plane with a horizontal ground surface boundary is also subject to the traction-free boundary condition as shown below

$$\mu \frac{\partial u_S(\mathbf{x})}{\partial y} = \mu \int \left[\frac{\partial T^E(\mathbf{s},\mathbf{x})}{\partial y} u_S(\mathbf{s}) - \frac{\partial U^E(\mathbf{s},\mathbf{x})}{\partial y} t_S(\mathbf{s})\right] \mathrm{d}B(\mathbf{s}) = 0,\ \mathbf{x} \in G, \tag{38}$$

where $\frac{\partial U^E(\mathbf{s},\mathbf{x})}{\partial y}$ and $\frac{\partial T^E(\mathbf{s},\mathbf{x})}{\partial y}$ are shown below

$$\frac{\partial U^E(\mathbf{s},\mathbf{x})}{\partial y} = \frac{1}{J_{\mathbf{x}}} c\cosh(\xi_{\mathbf{x}})\sin(\eta_{\mathbf{x}}) \frac{\partial U^E(\mathbf{s},\mathbf{x})}{\partial \xi_{\mathbf{x}}} + \frac{1}{J_{\mathbf{x}}} c\sinh(\xi_{\mathbf{x}})\cos(\eta_{\mathbf{x}}) \frac{\partial U^E(\mathbf{s},\mathbf{x})}{\partial \eta_{\mathbf{x}}}, \tag{39}$$

$$\frac{\partial T^E(\mathbf{s},\mathbf{x})}{\partial y} = \frac{1}{J_{\mathbf{x}}} c\cosh(\xi_{\mathbf{x}})\sin(\eta_{\mathbf{x}}) \frac{\partial T^E(\mathbf{s},\mathbf{x})}{\partial \xi_{\mathbf{x}}} + \frac{1}{J_{\mathbf{x}}} c\sinh(\xi_{\mathbf{x}})\cos(\eta_{\mathbf{x}}) \frac{\partial T^E(\mathbf{s},\mathbf{x})}{\partial \eta_{\mathbf{x}}}. \tag{40}$$

5 DISCRETIZATION TO A LINEAR ALGEBRAIC EQUATION

To calculate coefficients of eigenfunction expansion in eqs (28)–(31), $8M + 4$ boundary nodes for the real boundaries and artificial elliptical boundaries are needed.

5.1 Exterior problem by using the null-field BIEM

For the exterior problem containing an elliptical hole subject to the specified boundary condition as shown in Fig. 2(e), $2M + 1$ boundary nodes are needed and eq. (32) is discretized to

$$[\mathbf{T}^I]_{(2M+1)\times(2M+1)}\{\mathbf{u}^S\}_{(2M+1)\times 1} - [\mathbf{U}^I]_{(2M+1)\times(2M+1)}\{\mathbf{t}^S\}_{(2M+1)\times 1} = \{\mathbf{0}\}_{(2M+1)\times 1}, \tag{41}$$

where $[\mathbf{U}^I]$ and $[\mathbf{T}^I]$ are the influence matrices with a dimension of $2M+1$ by $2M+1$, $\{\mathbf{u}^S\}$ and $\{\mathbf{t}^S\}$ denote the column vectors of $u_S(\mathbf{s})$ and $t_S(\mathbf{s})$, for the generalized coordinates of eigenfunction expansion with a dimension of $2M+1$ by 1 as shown below

$$\{\mathbf{u}^S\} = \left\langle a_0^S \quad a_1^S \quad a_2^S \quad \cdots \quad a_M^S \quad b_1^S \quad b_2^S \quad \cdots \quad b_M^S \right\rangle^T, \tag{42}$$

$$\{\mathbf{t}^S\} = \left\langle p_0^S \quad p_1^S \quad p_2^S \quad \cdots \quad p_M^S \quad q_1^S \quad q_2^S \quad \cdots \quad q_M^S \right\rangle^T. \tag{43}$$

After uniformly collocating points in the direction of angular coordinate ($\eta_{\mathbf{x}}$) along the elliptical boundary, the influence matrices in eq. (32) can be written as

$$[\mathbf{U}^I] = \left[\begin{array}{ccc|ccc} U_1^I(\eta_{\mathbf{x}}^1) & \cdots & U_{M+1}^I(\eta_{\mathbf{x}}^1) & U_{M+2}^I(\eta_{\mathbf{x}}^1) & \cdots & U_{2M+1}^I(\eta_{\mathbf{x}}^1) \\ U_1^I(\eta_{\mathbf{x}}^2) & \cdots & U_{M+1}^I(\eta_{\mathbf{x}}^2) & U_{M+2}^I(\eta_{\mathbf{x}}^2) & \cdots & U_{2M+1}^I(\eta_{\mathbf{x}}^2) \\ \vdots & \ddots & \vdots & \vdots & \ddots & \vdots \\ U_1^I(\eta_{\mathbf{x}}^{2M}) & \cdots & U_{M+1}^I(\eta_{\mathbf{x}}^{2M}) & U_{M+2}^I(\eta_{\mathbf{x}}^{2M}) & \cdots & U_{2M+1}^I(\eta_{\mathbf{x}}^{2M}) \\ U_1^I(\eta_{\mathbf{x}}^{2M+1}) & \cdots & U_{M+1}^I(\eta_{\mathbf{x}}^{2M+1}) & U_{M+2}^I(\eta_{\mathbf{x}}^{2M+1}) & \cdots & U_{2M+1}^I(\eta_{\mathbf{x}}^{2M+1}) \end{array}\right], \tag{44}$$

$$[\mathbf{T}^I] = \left[\begin{array}{ccc|ccc} T_1^I(\eta_{\mathbf{x}}^1) & \cdots & T_{M+1}^I(\eta_{\mathbf{x}}^1) & T_{M+2}^I(\eta_{\mathbf{x}}^1) & \cdots & T_{2M+1}^I(\eta_{\mathbf{x}}^1) \\ T_1^I(\eta_{\mathbf{x}}^2) & \cdots & T_{M+1}^I(\eta_{\mathbf{x}}^2) & T_{M+2}^I(\eta_{\mathbf{x}}^2) & \cdots & T_{2M+1}^I(\eta_{\mathbf{x}}^2) \\ \vdots & \ddots & \vdots & \vdots & \ddots & \vdots \\ T_1^I(\eta_{\mathbf{x}}^{2M}) & \cdots & T_{M+1}^I(\eta_{\mathbf{x}}^{2M}) & T_{M+2}^I(\eta_{\mathbf{x}}^{2M}) & \cdots & T_{2M+1}^I(\eta_{\mathbf{x}}^{2M}) \\ T_1^I(\eta_{\mathbf{x}}^{2M+1}) & \cdots & T_{M+1}^I(\eta_{\mathbf{x}}^{2M+1}) & T_{M+2}^I(\eta_{\mathbf{x}}^{2M+1}) & \cdots & T_{2M+1}^I(\eta_{\mathbf{x}}^{2M+1}) \end{array}\right], \tag{45}$$

where the elements of $[\mathbf{U}^I]$ and $[\mathbf{T}^I]$ are defined respectively as

$$U_n^I(\eta_{\mathbf{x}}^L) = \int_0^{2\pi} U^I(\mathbf{s}, \mathbf{x}_L) Se_{n-1}(q,\ \eta_{\mathbf{s}})\, \mathrm{d}\eta_{\mathbf{s}}, \tag{46}$$

$$U_{M+1+\bar{n}}^I(\eta_{\mathbf{x}}^L) = \int_0^{2\pi} U^I(\mathbf{s}, \mathbf{x}_L) So_{\bar{n}}(q,\ \eta_{\mathbf{s}})\, \mathrm{d}\eta_{\mathbf{s}}, \tag{47}$$

$$T_n^I(\eta_{\mathbf{x}}^L) = \int_0^{2\pi} T^I(\mathbf{s}, \mathbf{x}_L) Se_{n-1}(q,\ \eta_{\mathbf{s}}) J_{\mathbf{s}}\, \mathrm{d}\eta_{\mathbf{s}}, \tag{48}$$

$$T_{M+1+\bar{n}}^I(\eta_{\mathbf{x}}^L) = \int_0^{2\pi} T^I(\mathbf{s}, \mathbf{x}_L) So_{\bar{n}}(q,\ \eta_{\mathbf{s}}) J_{\mathbf{s}}\, \mathrm{d}\eta_{\mathbf{s}}, \tag{49}$$

where $n = 1, 2, \ldots, M+1$, $\bar{n} = 1, 2, \ldots, M$, $L = 1, 2, \ldots, 2M+1$ and $\eta_{\mathbf{x}}^L$ is the angular coordinate of the collocation point $\mathbf{x}_L$ in the elliptical coordinates.

5.2 Interior problem by using the null-field BIEM

By uniformly collocating $2M+1$ boundary nodes for the region II in Fig. 2(c), eq. (33) is discretized to

$$[\mathbf{T}^E]_{(2M+1)\times(2M+1)}\{\mathbf{u}^H\}_{(2M+1)\times 1} - [\mathbf{U}^E]_{(2M+1)\times(2M+1)}\{\mathbf{t}^H\}_{(2M+1)\times 1} = \{\mathbf{0}\}_{(2M+1)\times 1}, \tag{50}$$

where $\{\mathbf{u}^H\}$ and $\{\mathbf{t}^H\}$ denote the column vectors of $u_{\mathrm{H}}(\mathbf{s})$ and $t_H(\mathbf{s})$, for the generalized coordinates of eigenfunction expansion as shown below

$$\{\mathbf{u}^H\} = \left\langle a_0^H \quad a_1^H \quad a_2^H \quad \cdots \quad a_M^H \quad b_1^H \quad b_2^H \quad \cdots \quad b_M^H \right\rangle^T, \tag{51}$$

$$\{\mathbf{t}^H\} = \left\langle p_0^H \quad p_1^H \quad p_2^H \quad \cdots \quad p_M^H \quad q_1^H \quad q_2^H \quad \cdots \quad q_M^H \right\rangle^T, \tag{52}$$

$[\mathbf{U}^E]$ and $[\mathbf{T}^E]$ are

$$[\mathbf{U}^E] = \left[\begin{array}{ccc|ccc} U_1^E(\eta_{\mathbf{x}}^1) & \cdots & U_{M+1}^E(\eta_{\mathbf{x}}^1) & U_{M+2}^E(\eta_{\mathbf{x}}^1) & \cdots & U_{2M+1}^E(\eta_{\mathbf{x}}^1) \\ U_1^E(\eta_{\mathbf{x}}^2) & \cdots & U_{M+1}^E(\eta_{\mathbf{x}}^2) & U_{M+2}^E(\eta_{\mathbf{x}}^2) & \cdots & U_{2M+1}^E(\eta_{\mathbf{x}}^2) \\ \vdots & \ddots & \vdots & \vdots & \ddots & \vdots \\ U_1^E(\eta_{\mathbf{x}}^{2M}) & \cdots & U_{M+1}^E(\eta_{\mathbf{x}}^{2M}) & U_{M+2}^E(\eta_{\mathbf{x}}^{2M}) & \cdots & U_{2M+1}^E(\eta_{\mathbf{x}}^{2M}) \\ U_1^E(\eta_{\mathbf{x}}^{2M+1}) & \cdots & U_{M+1}^E(\eta_{\mathbf{x}}^{2M+1}) & U_{M+2}^E(\eta_{\mathbf{x}}^{2M+1}) & \cdots & U_{2M+1}^E(\eta_{\mathbf{x}}^{2M+1}) \end{array}\right], \tag{53}$$

$$[\mathbf{T}^E] = \left[\begin{array}{ccc|ccc} T_1^E(\eta_{\mathbf{x}}^1) & \cdots & T_{M+1}^E(\eta_{\mathbf{x}}^1) & T_{M+2}^E(\eta_{\mathbf{x}}^1) & \cdots & T_{2M+1}^E(\eta_{\mathbf{x}}^1) \\ T_1^E(\eta_{\mathbf{x}}^2) & \cdots & T_{M+1}^E(\eta_{\mathbf{x}}^2) & T_{M+2}^E(\eta_{\mathbf{x}}^2) & \cdots & T_{2M+1}^E(\eta_{\mathbf{x}}^2) \\ \vdots & \ddots & \vdots & \vdots & \ddots & \vdots \\ T_1^E(\eta_{\mathbf{x}}^{2M}) & \cdots & T_{M+1}^E(\eta_{\mathbf{x}}^{2M}) & T_{M+2}^E(\eta_{\mathbf{x}}^{2M}) & \cdots & T_{2M+1}^E(\eta_{\mathbf{x}}^{2M}) \\ T_1^E(\eta_{\mathbf{x}}^{2M+1}) & \cdots & T_{M+1}^E(\eta_{\mathbf{x}}^{2M+1}) & T_{M+2}^E(\eta_{\mathbf{x}}^{2M+1}) & \cdots & T_{2M+1}^E(\eta_{\mathbf{x}}^{2M+1}) \end{array}\right], \tag{54}$$

in which the elements of $[\mathbf{U}^E]$ and $[\mathbf{T}^E]$ are defined, respectively, as

$$U_n^E(\eta_{\mathbf{x}}^L) = \int_0^{2\pi} U^E(\mathbf{s}, \mathbf{x}_L) Se_{n-1}(q,\ \eta_{\mathbf{s}})\, \mathrm{d}\eta_{\mathbf{s}}, \tag{55}$$

$$U_{M+1+\bar{n}}^E(\eta_{\mathbf{x}}^L) = \int_0^{2\pi} U^E(\mathbf{s}, \mathbf{x}_L) So_{\bar{n}}(q,\ \eta_{\mathbf{s}})\, \mathrm{d}\eta_{\mathbf{s}}, \tag{56}$$

$$T_n^E(\eta_{\mathbf{x}}^L) = \int_0^{2\pi} T^E(\mathbf{s}, \mathbf{x}_L) Se_{n-1}(q,\ \eta_{\mathbf{s}}) J_{\mathbf{s}}\, \mathrm{d}\eta_{\mathbf{s}}, \tag{57}$$

$$T_{M+1+\bar{n}}^E(\eta_{\mathbf{x}}^L) = \int_0^{2\pi} T^E(\mathbf{s}, \mathbf{x}_L) So_{\bar{n}}(q,\ \eta_{\mathbf{s}}) J_{\mathbf{s}}\, \mathrm{d}\eta_{\mathbf{s}}, \tag{58}$$

where $n = 1, 2, \ldots, M+1$, $\bar{n} = 1, 2, \ldots, M$, $L = 1, 2, \ldots, 2M+1$ and $\eta_{\mathbf{x}}^L$ is the angular coordinate of the collocation point $\mathbf{x}_L$ in the elliptic coordinates.

5.3 Continuity condition on the artificial interface

By matching the continuity condition on the artificial interface ($\overline{G}$ or $\overline{H}$), eq. (34) can be rewritten as

$$u_S(\eta_{\mathbf{x}}) - u_H(\eta_{\mathbf{x}}) = -\left[u_I(\eta_{\mathbf{x}}) + u_R(\eta_{\mathbf{x}})\right],\ \pi \le \eta_{\mathbf{x}} \le 2\pi, \tag{59}$$

by collocating N_{ai} nodes on the artificial interface, and we have

$$[\mathbf{Q}_{ai}]_{N_{ai}\times(2M+1)} \{\mathbf{u}^S\}_{(2M+1)\times 1} - [\mathbf{Q}_{ai}]_{N_{ai}\times(2M+1)} \{\mathbf{u}^H\}_{(2M+1)\times 1} = -\{\mathbf{u}_I + \mathbf{u}_R\}_{N_{ai}\times 1}, \tag{60}$$

where N_{ai} is the number of boundary nodes on the artificial interface as shown in Fig. 3 and $[\mathbf{Q}_{ai}]$ is defined by

$$[\mathbf{Q}_{ai}] = \left[\begin{array}{cccccc} Se_0(q, \eta_{\mathbf{x}}^1) & Se_1(q, \eta_{\mathbf{x}}^1) & \cdots & Se_M(q, \eta_{\mathbf{x}}^1) & So_1(q, \eta_{\mathbf{x}}^1) & \cdots & So_M(q, \eta_{\mathbf{x}}^1) \\ Se_0(q, \eta_{\mathbf{x}}^2) & Se_1(q, \eta_{\mathbf{x}}^2) & \cdots & Se_M(q, \eta_{\mathbf{x}}^2) & So_1(q, \eta_{\mathbf{x}}^2) & \cdots & So_M(q, \eta_{\mathbf{x}}^2) \\ \vdots & \vdots & \ddots & \vdots & \vdots & \ddots & \vdots \\ Se_0(q, \eta_{\mathbf{x}}^{N_{ai}-1}) & Se_1(q, \eta_{\mathbf{x}}^{N_{ai}-1}) & \cdots & Se_M(q, \eta_{\mathbf{x}}^{N_{ai}-1}) & So_1(q, \eta_{\mathbf{x}}^{N_{ai}-1}) & \cdots & So_M(q, \eta_{\mathbf{x}}^{N_{ai}-1}) \\ Se_0(q, \eta_{\mathbf{x}}^{N_{ai}}) & Se_1(q, \eta_{\mathbf{x}}^{N_{ai}}) & \cdots & Se_M(q, \eta_{\mathbf{x}}^{N_{ai}}) & So_1(q, \eta_{\mathbf{x}}^{N_{ai}}) & \cdots & So_M(q, \eta_{\mathbf{x}}^{N_{ai}}) \end{array}\right]. \tag{61}$$

5.4 Equilibrium condition on the artificial interface

By matching the equilibrium condition on the artificial interface ($\overline{G}$ or $\overline{H}$), eq. (36) can be rewritten as

$$\tau_S(\eta_{\mathbf{x}}) + \tau_H(\eta_{\mathbf{x}}) = -\left[\tau_I(\eta_{\mathbf{x}}) + \tau_R(\eta_{\mathbf{x}})\right],\ \pi \le \eta_{\mathbf{x}} \le 2\pi. \tag{62}$$

Similarly, collocation N_{ai} nodes yields

$$\frac{1}{J_{\mathbf{x}}} [\mathbf{Q}_{ai}]_{N_{ai}\times(2M+1)} \{\mathbf{t}^S\}_{(2M+1)\times 1} + \frac{1}{J_{\mathbf{x}}} [\mathbf{Q}_{ai}]_{N_{ai}\times(2M+1)} \{\mathbf{t}^H\}_{(2M+1)\times 1} = -\{\mathbf{t}_I + \mathbf{t}_R\}_{N_{ai}\times 1}, \tag{63}$$

where $[\mathbf{Q}_{ai}]$ is the same with eq. (61).

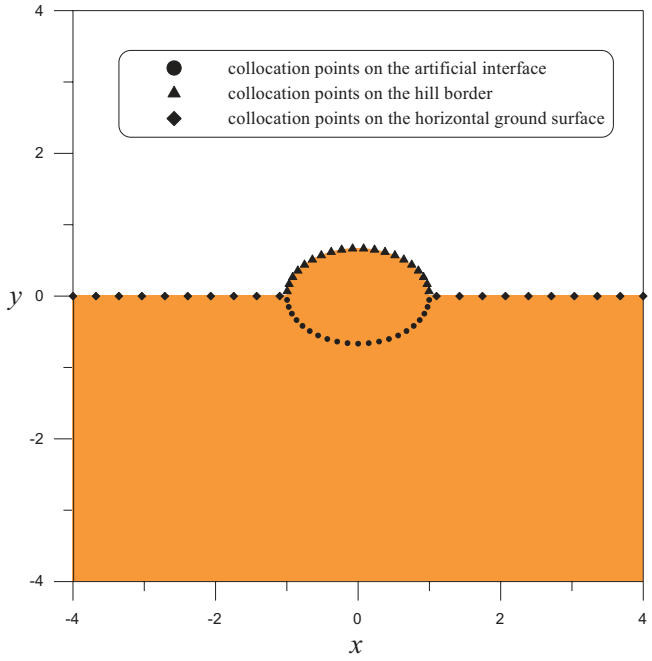

Figure 3. Distribution of collocation points for the semi-elliptical hill scattering problem.

5.5 Boundary condition on the hill border

By distributing N_{hb} collocation points at the hill border of Region II in eq. (37), we have

$$[\mathbf{Q}_{hb}]_{N_{hb}\times(2M+1)}\{\mathbf{t}^H\}_{(2M+1)\times 1}=\{\mathbf{0}\}_{N_{hb}\times 1}, \tag{64}$$

where N_{hb} is the number of collocation points on the hill border (H) as shown in Fig. 3 and $[\mathbf{Q}_{hb}]$ is

$$[\mathbf{Q}_{hb}]=\begin{bmatrix} Se_0(q,\eta_{\mathbf{x}}^1) & Se_1(q,\eta_{\mathbf{x}}^1) & \cdots & Se_M(q,\eta_{\mathbf{x}}^1) & So_1(q,\eta_{\mathbf{x}}^1) & \cdots & So_M(q,\eta_{\mathbf{x}}^1) \\ Se_0(q,\eta_{\mathbf{x}}^2) & Se_1(q,\eta_{\mathbf{x}}^2) & \cdots & Se_M(q,\eta_{\mathbf{x}}^2) & So_1(q,\eta_{\mathbf{x}}^2) & \cdots & So_M(q,\eta_{\mathbf{x}}^2) \\ \vdots & \vdots & \ddots & \vdots & \vdots & \ddots & \vdots \\ Se_0(q,\eta_{\mathbf{x}}^{N_{hb}-1}) & Se_1(q,\eta_{\mathbf{x}}^{N_{hb}-1}) & \cdots & Se_M(q,\eta_{\mathbf{x}}^{N_{hb}-1}) & So_1(q,\eta_{\mathbf{x}}^{N_{hb}-1}) & \cdots & So_M(q,\eta_{\mathbf{x}}^{N_{hb}-1}) \\ Se_0(q,\eta_{\mathbf{x}}^{N_{hb}}) & Se_1(q,\eta_{\mathbf{x}}^{N_{hb}}) & \cdots & Se_M(q,\eta_{\mathbf{x}}^{N_{hb}}) & So_1(q,\eta_{\mathbf{x}}^{N_{hb}}) & \cdots & So_M(q,\eta_{\mathbf{x}}^{N_{hb}}) \end{bmatrix}. \tag{65}$$

5.6 Boundary condition on the horizontal ground surface

By collocating N_{hgs} nodes to match the traction-free boundary conditions along the horizontal ground surface in eq. (38), we have

$$[\mathbf{T}_y^E]_{N_{\mathbf{hgs}}\times(2M+1)}\{\mathbf{u}^S\}_{(2M+1)\times 1}-[\mathbf{U}_y^E]_{N_{\mathbf{hgs}}\times(2M+1)}\{\mathbf{t}^S\}_{(2M+1)\times 1}=\{\mathbf{0}\}_{N_{\mathbf{hgs}}\times 1}, \tag{66}$$

where

$$[\mathbf{U}_y^E]=\left[\begin{array}{ccc|ccc} U_{y1}^E(\eta_{\mathbf{x}}^1) & \cdots & U_{y(M+1)}^E(\eta_{\mathbf{x}}^1) & U_{y(M+2)}^E(\eta_{\mathbf{x}}^1) & \cdots & U_{y(2M+1)}^E(\eta_{\mathbf{x}}^1) \\ U_{y1}^E(\eta_{\mathbf{x}}^2) & \cdots & U_{y(M+1)}^E(\eta_{\mathbf{x}}^2) & U_{y(M+2)}^E(\eta_{\mathbf{x}}^2) & \cdots & U_{y(2M+1)}^E(\eta_{\mathbf{x}}^2) \\ \vdots & \ddots & \vdots & \vdots & \ddots & \vdots \\ U_{y1}^E(\eta_{\mathbf{x}}^{2M}) & \cdots & U_{y(M+1)}^E(\eta_{\mathbf{x}}^{2M}) & U_{y(M+2)}^E(\eta_{\mathbf{x}}^{2M}) & \cdots & U_{y(2M+1)}^E(\eta_{\mathbf{x}}^{2M}) \\ U_{y1}^E(\eta_{\mathbf{x}}^{2M+1}) & \cdots & U_{y(M+1)}^E(\eta_{\mathbf{x}}^{2M+1}) & U_{y(M+2)}^E(\eta_{\mathbf{x}}^{2M+1}) & \cdots & U_{y(2M+1)}^E(\eta_{\mathbf{x}}^{2M+1}) \end{array}\right], \tag{67}$$

$$[\mathbf{T}_y^E]=\left[\begin{array}{ccc|ccc} T_{y1}^E(\eta_{\mathbf{x}}^1) & \cdots & T_{y(M+1)}^E(\eta_{\mathbf{x}}^1) & T_{y(M+2)}^E(\eta_{\mathbf{x}}^1) & \cdots & T_{y(2M+1)}^E(\eta_{\mathbf{x}}^1) \\ T_{y1}^E(\eta_{\mathbf{x}}^2) & \cdots & T_{y(M+1)}^E(\eta_{\mathbf{x}}^2) & T_{y(M+2)}^E(\eta_{\mathbf{x}}^2) & \cdots & T_{y(2M+1)}^E(\eta_{\mathbf{x}}^2) \\ \vdots & \ddots & \vdots & \vdots & \ddots & \vdots \\ T_{y1}^E(\eta_{\mathbf{x}}^{2M}) & \cdots & T_{y(M+1)}^E(\eta_{\mathbf{x}}^{2M}) & T_{y(M+2)}^E(\eta_{\mathbf{x}}^{2M}) & \cdots & T_{y(2M+1)}^E(\eta_{\mathbf{x}}^{2M}) \\ T_{y1}^E(\eta_{\mathbf{x}}^{2M+1}) & \cdots & T_{y(M+1)}^E(\eta_{\mathbf{x}}^{2M+1}) & T_{y(M+2)}^E(\eta_{\mathbf{x}}^{2M+1}) & \cdots & T_{y(2M+1)}^E(\eta_{\mathbf{x}}^{2M+1}) \end{array}\right], \tag{68}$$

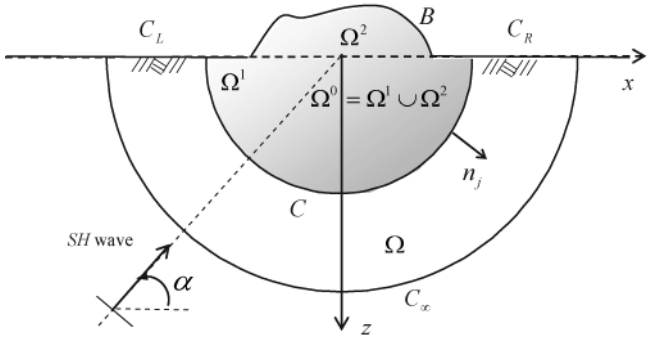

Figure 4. An arbitrary-shape hill embedded into an elastic half-space.

in which the subscript of y is the partial differential operator in the y direction, $N_{\rm hgs}$ is the number of collocation points on the horizontal ground surface (G) as shown in Fig. 3 and the elements of $[\mathbf{U}_y^E]$ and $[\mathbf{T}_y^E]$ are defined respectively as

$$U_{yn}^E(\eta_{\mathbf{x}}^{\bar{L}}) = \int_0^{2\pi} U_y^E(\mathbf{s}, \mathbf{x}_{\bar{L}}) Se_{n-1}(q,\ \eta_{\mathbf{s}})\, \mathrm{d}\eta_{\mathbf{s}}, \tag{69}$$

$$U_{y(M+1+\bar{n})}^E(\eta_{\mathbf{x}}^{\bar{L}}) = \int_0^{2\pi} U_y^E(\mathbf{s}, \mathbf{x}_{\bar{L}}) So_{\bar{n}}(q,\ \eta_{\mathbf{s}})\, \mathrm{d}\eta_{\mathbf{s}}, \tag{70}$$

$$T_{yn}^E(\eta_{\mathbf{x}}^{\bar{L}}) = \int_0^{2\pi} T_y^E(\mathbf{s}, \mathbf{x}_{\bar{L}}) Se_{n-1}(q,\ \eta_{\mathbf{s}}) J_{\mathbf{s}}\, \mathrm{d}\eta_{\mathbf{s}}, \tag{71}$$

$$T_{y(M+1+\bar{n})}^E(\eta_{\mathbf{x}}^{\bar{L}}) = \int_0^{2\pi} T_y^E(\mathbf{s}, \mathbf{x}_{\bar{L}}) So_{\bar{n}}(q,\ \eta_{\mathbf{s}}) J_{\mathbf{s}}\, \mathrm{d}\eta_{\mathbf{s}}, \tag{72}$$

where $n = 1, 2, \ldots, M+1$, $\bar{n} = 1, 2, \ldots, M$, $\bar{L} = 1, 2, \ldots, N_{\mathbf{hgs}}$.

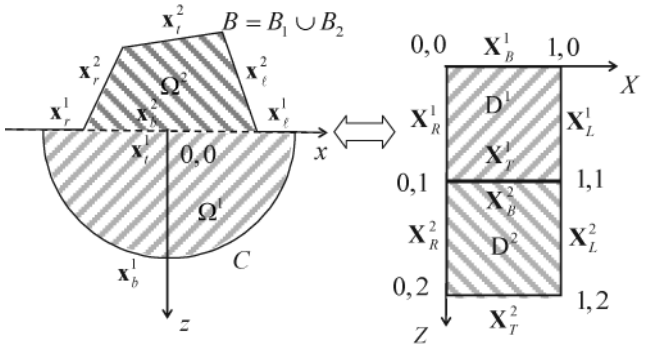

Figure 5. A regular hill and its mapping function.

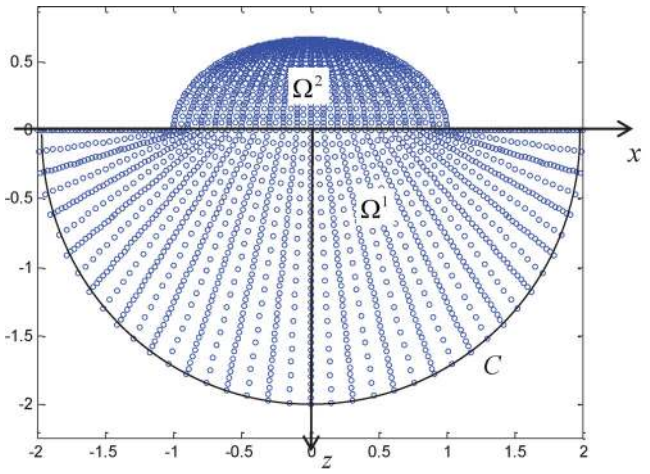

Figure 6. Mesh distribution of the hybrid method for a semi-elliptical hill.

Table 1. Parameters of the hill scattering model.

Type	Case 1 Shallow hill	Case 2 Deep hill
Half width and height (a, b)	$a = 1,\ b = 2/3$	$a = 1,\ b = 4/3$
Shear modulus (μ)	$\mu = 1$	
Dimensionless frequency (η)	$\eta = 0.5$ or 2	
Incident angle (α)	$\alpha = 0^\circ$, 30°, 60° or 90°	

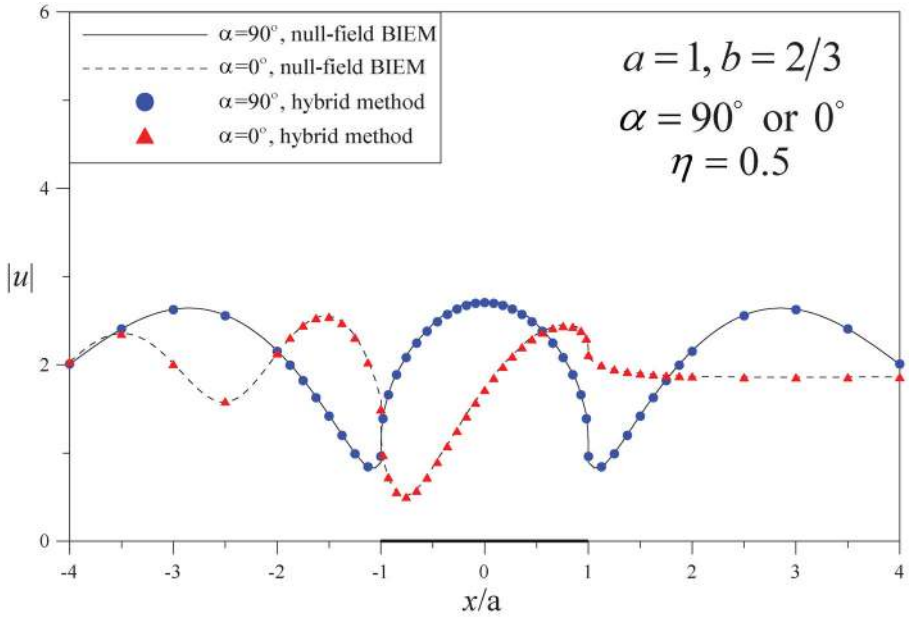

Figure 7. Surface displacement amplitudes versus x/a for the case 1 of dimensionless frequency $\eta = 0.5$. (a) $\alpha = 90^\circ$ and 0° and (b) $\alpha = 30^\circ$ and 60°.

By assembling eqs (41), (50), (60), (63), (64) and (66) together, we have

$$\begin{bmatrix} \mathbf{T}^I & -\mathbf{U}^I & \mathbf{0} & \mathbf{0} \\ \mathbf{0} & \mathbf{0} & \mathbf{T}^E & -\mathbf{U}^E \\ \mathbf{Q}_{ai} & \mathbf{0} & -\mathbf{Q}_{ai} & \mathbf{0} \\ \mathbf{0} & \mathbf{Q}_{ai} & \mathbf{0} & \mathbf{Q}_{ai} \\ \mathbf{0} & \mathbf{0} & \mathbf{0} & \mathbf{Q}_{hb} \\ \mathbf{T}^E_{\mathrm{y}} & -\mathbf{U}^E_{\mathrm{y}} & \mathbf{0} & \mathbf{0} \end{bmatrix}_{(8M+4)\times(8M+4)} \begin{Bmatrix} \mathbf{u}^S \\ \mathbf{t}^S \\ \mathbf{u}^H \\ \mathbf{t}^H \end{Bmatrix}_{(8M+4)\times 1} = \begin{Bmatrix} \mathbf{0} \\ \mathbf{0} \\ -\mathbf{u}_I - \mathbf{u}_R \\ -\mathbf{t}_I - \mathbf{t}_R \\ \mathbf{0} \\ \mathbf{0} \end{Bmatrix}_{(8M+4)\times 1}, \tag{73}$$

where $2N_{ai} + N_{hb} + N_{\mathrm{hgs}} = 4M + 2$. According to the linear algebraic equation in eq. (73), all coefficients in the eigenfunction expansion can be easily obtained.

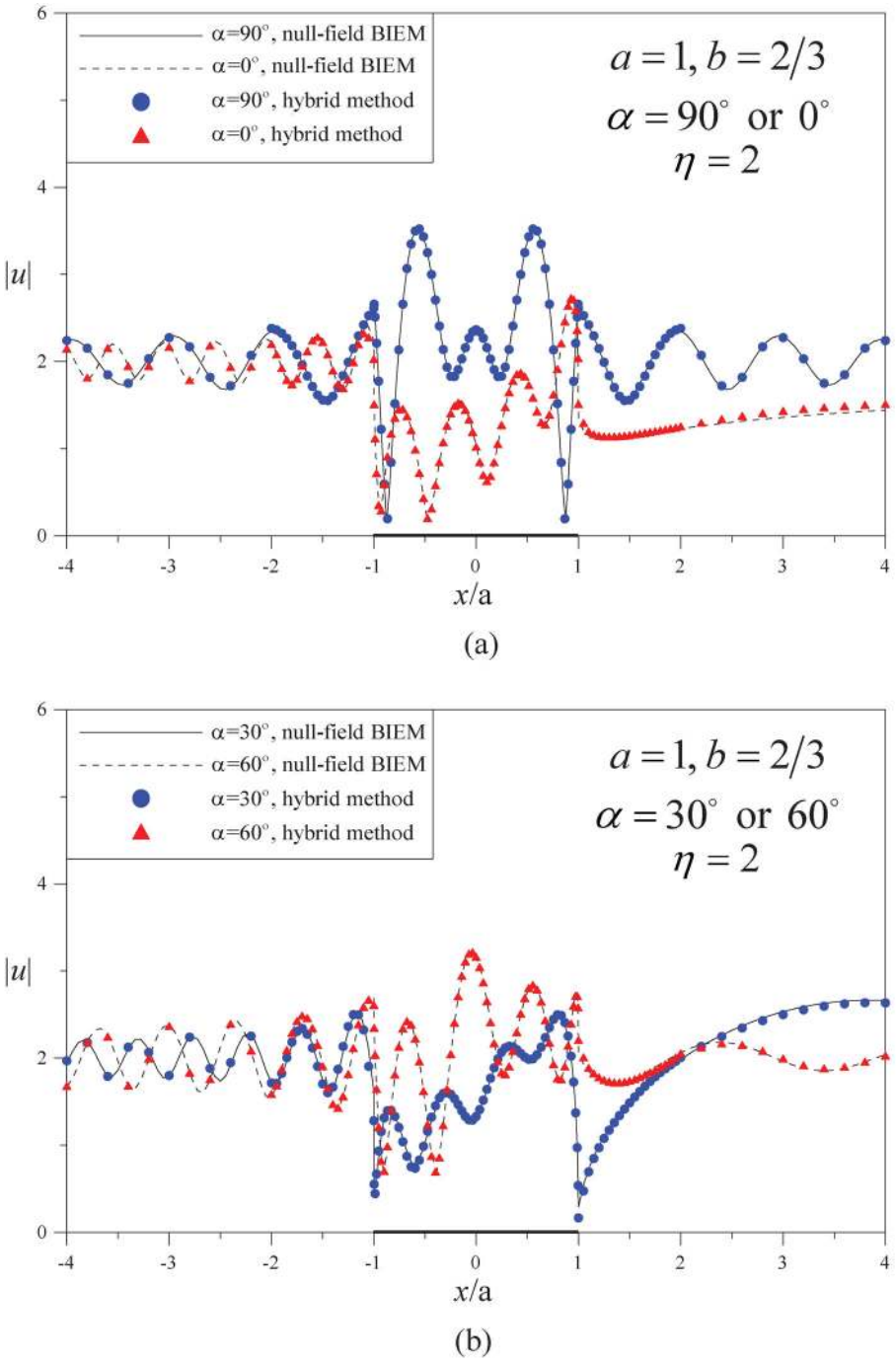

Figure 8. Surface displacement amplitudes versus *x/a* for the case 1 of dimensionless frequency $\eta = 2$. (a) $\alpha = 90^\circ$ and 0° and (b) $\alpha = 30^\circ$ and 60°.

6 HYBRID METHOD

To verify the validity of the null-field BIEM, an alternative approach using the hybrid method is described here. The response of surface motion inside and near an arbitrary hill in an elastic half-plane is investigated for the case of incident *SH* wave as shown in Fig. 4. Based on a variational formalism proposed by Mei (1980), a hybrid method combining the finite element and series-expansion method was implemented to solve the scattering problems. Yeh *et al.* (2000a,b, 2002, 2007) have extended the hybrid method to solve the problems of scattering wave by canyons, alluvial valleys or cavities (shells) buried in an elastic half-plane, where the hybrid method was discussed in detail.

We define a substructure Ω^0 enclosing the arbitrary hill. It can be easily formulated by using the finite element method. The unknown boundary data are obtained by subtracting the known free fields from the total fields which include the boundary nodal displacements and

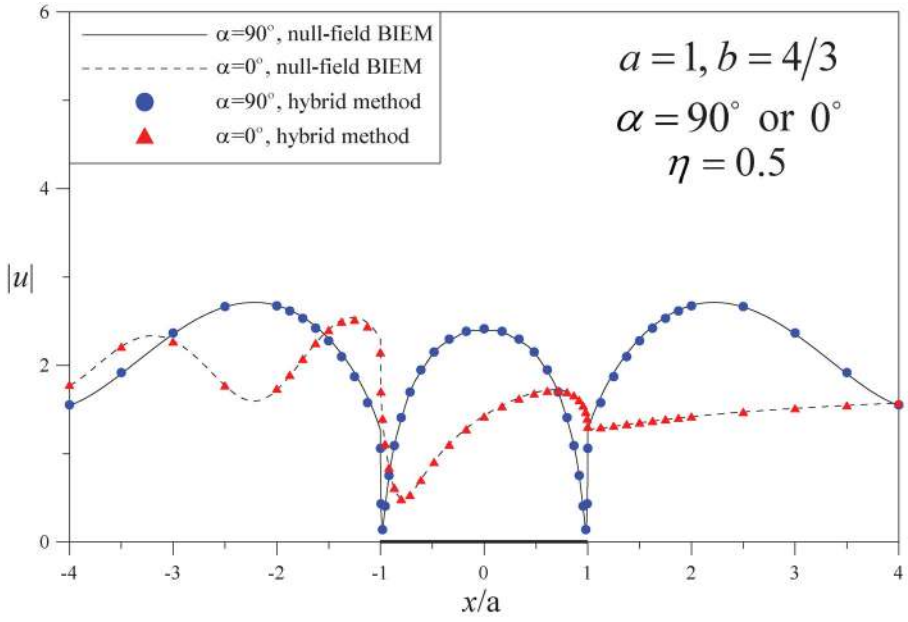

Figure 9. Surface displacement amplitudes versus *x/a* for the case 2 of dimensionless frequency $\eta = 0.5$. (a) $\alpha = 90^\circ$ and 0° and (b) $\alpha = 30^\circ$ and 60°.

tractions at the interface between the finite domain and the surrounding elastic half-space. It is shown in a matrix form as given below:

$$\begin{bmatrix} \mathbf{K}^{aa} - \omega^2 \mathbf{M}^{aa} & -\mathbf{K}^{ac} \\ -\mathbf{K}^{ca} & \mathbf{K}^{cc} \end{bmatrix} \begin{Bmatrix} \mathbf{a} \\ \mathbf{c} \end{Bmatrix} = \begin{Bmatrix} \mathbf{P}^a \\ -\mathbf{P}^c \end{Bmatrix}. \tag{74}$$

The arbitrary finite domain Ω^0 is mapped into a rectangular domain as shown in Fig. 5 and its finite element meshes are discretized in the rectangular domain. Therefore, the displacement field in each element can be represented by the vector of nodal displacement {**a**}. The scattered waves can be formulated through a series representation with unknown coefficients {**c**}. The expansion function of the series representation is constituted of basis function. Each basis function is constructed by using Lamb's solution and satisfies both traction-free condition on the ground surface and radiation condition at infinity.

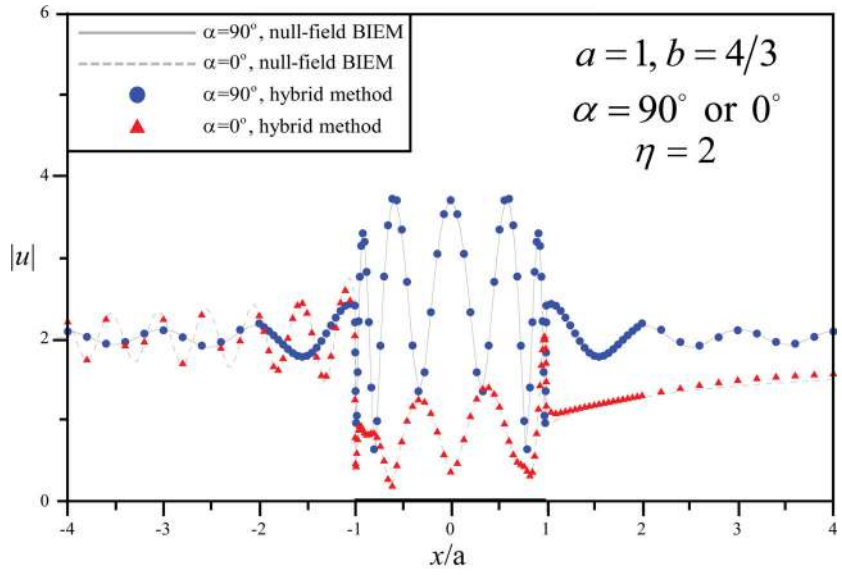

(a)

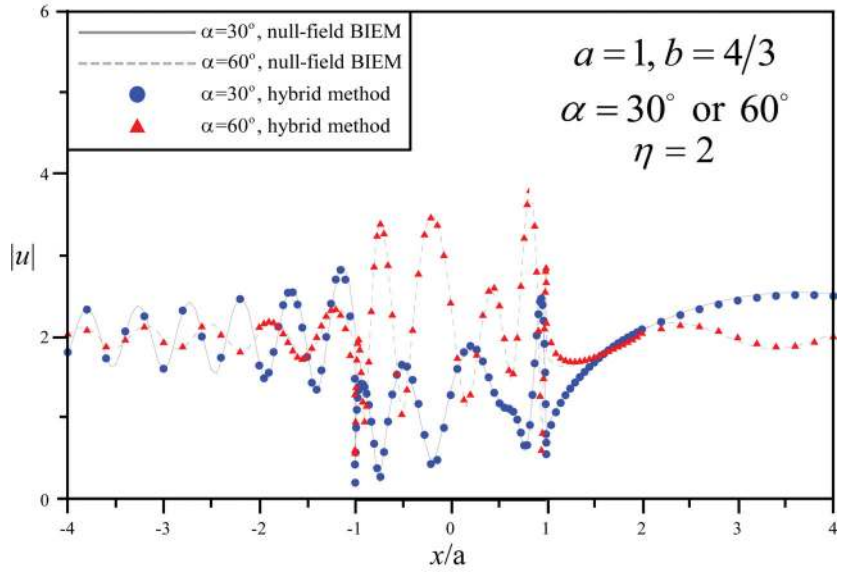

(b)

Figure 10. Surface displacement amplitudes versus *x/a* for the case 2 of dimensionless frequency $\eta = 2$. (a) $\alpha = 90^\circ$ and 0° and (b) $\alpha = 30^o$ and 60^o.

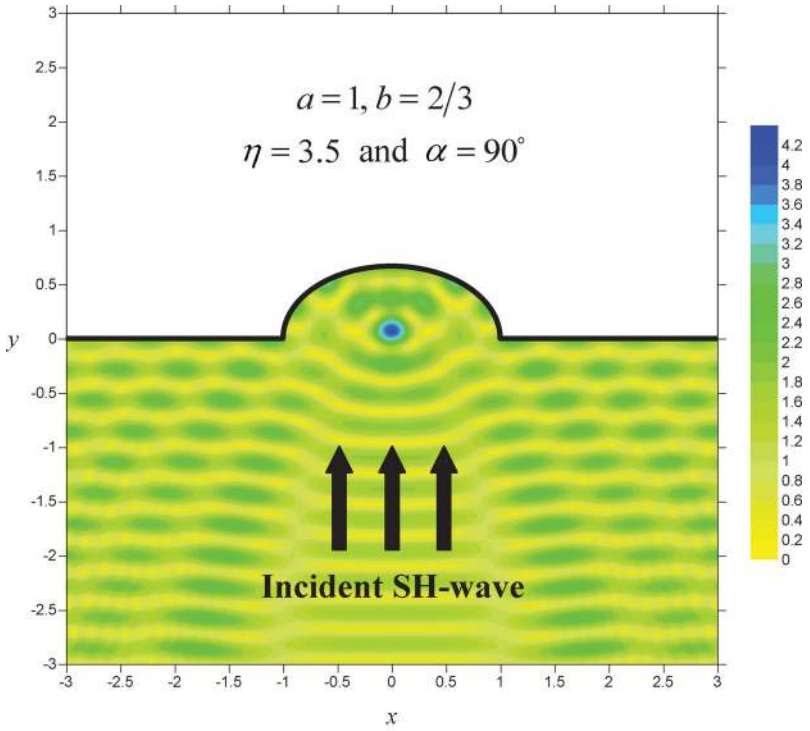

(a)

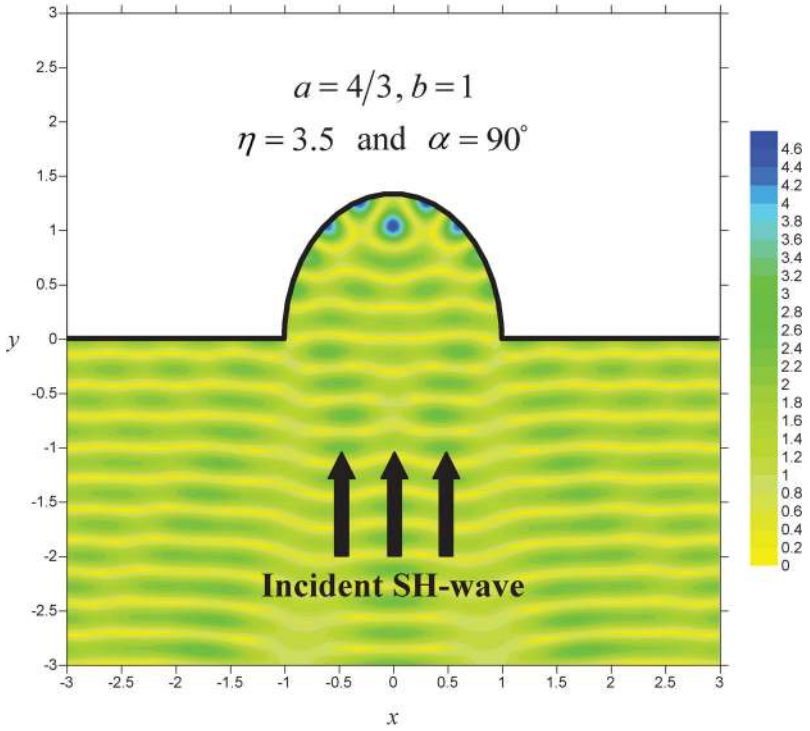

(b)

Figure 11. Focusing effect in the contour plot of displacement amplitude for $\eta = 3.5$ and the incident angle of $\alpha = 90^{\circ}$. (a) case 1 (shallow hill) and (b) case 2 (deep hill).

The merit of the hybrid method is that the flexibility of finite elements offers the greatest advantage to model the arbitrary-shape hills, for example, a semi-elliptical hill in this paper. We use a simple mapping function to calculate the coordinates of the elliptical hill. The node numbers of the finite elements and the arrangement of the elements are the same for different shape hills. The mapping function (Tompson 1985) is

$$\mathbf{x} = (1-Z)\,\mathbf{x}_b^j + Z\mathbf{x}_t^j + (1-Z)\,\mathbf{x}_\ell^j + X\mathbf{x}_r^j - XZ\mathbf{x}_t^j + X(1-Z)\,\mathbf{x}_b^j + Z(1-X)\,\mathbf{x}_t^j(1) + (1-X)(1-Z)\,\mathbf{x}_b^j(1), \tag{75}$$

where $j = 1$, $\mathbf{X} = (X, Z)$ and $0 \le X, Z \le 1$; $j = 2$, $\mathbf{X} = (X, Z)$ and $0 \le X \le 1$, $1 \le Z \le 2$, $\mathbf{x}_b^j$, $\mathbf{x}_t^j$, $\mathbf{x}_\ell^j$, and $\mathbf{x}_r^j$ are shown in Fig. 5. Fig. 6 shows a semi-elliptical hill for $b/a = 2/3$, where $a = 1$ and $b = 2/3$ are the half width and height of the semi-elliptical hill, respectively. We use 800 Q8 elements and 2521 nodes to mesh the irregular region as shown in Fig. 6. Some results will be compared with those obtained by using the null-field BIEM in the following section of numerical examples.

7 A NUMERICAL EXAMPLE

A benchmark example of semi-elliptical hill is considered. The dimensionless frequency η is defined by

$$\eta = \frac{\omega a}{\pi c_s} = \frac{ka}{\pi} = \frac{2a}{\lambda}, \tag{76}$$

where ω is the angular frequency, c_s is the velocity of shear wave, λ is the length of shear wave. The displacement amplitude is an important index for the earthquake engineering. If the amplitude of incident plane *SH* wave is assumed to be one, $A_0 = 1$, the responses at different locations represent amplifications of the incident plane *SH* wave. The displacement amplitude is defined by

$$|u| = \begin{cases} |u_I + u_R + u_S|, & \text{for the region I,} \\ |u_H|, & \text{for the region II.} \end{cases} \tag{77}$$

Here, we consider two cases of semi-elliptical hill subject to a *SH* wave. The corresponding parameters are shown in Table 1. Figs 7 and 8 show the surface displacement amplitude versus x/a of the case 1 for the dimensionless frequency $\eta = 0.5$ and 2, respectively. The corresponding position of the hill border is within the range of $x/a = -1.0$ to 1.0 (bold line). After comparing with the results of the hybrid method, a good agreement is made. Similarly, the surface displacement amplitude versus x/a of the case 2 are shown in Figs 9 and 10 for $\eta = 0.5$ and 2, respectively. Parameter study of dimensionless frequency and incident angle is considered. All numerical results are obtained by using the null-field BIEM and are compared well with those of the hybrid method.

Besides, it is interesting to find that large displacement amplitude is observed in a localized area for the case of incident angle $\alpha = 90^\circ$ and $\eta = 3.5$ in Fig. 11. This phenomenon is the so-called focusing as well as in optics and acoustics. The similar phenomenon for a shallow circular hill has been found by Tsaur & Chang (2009) in both time and frequency domains. Besides, this focusing effect was also observed in the semi-circular hill by Chen *et al*. (2011b).

8 CONCLUSIONS

In this paper, the *SH*-wave problem scattered by a semi-elliptical hill was solved. By taking free body, the original problem can be decomposed to two subdomains. For the half-plane with a half-elliptical arc, it is designed to be imbedded in an infinite domain with an elliptical boundary. Thanks to an elliptical boundary, we naturally employed the null-field BIEM in conjunction with the degenerate kernel and eigenfunction expansion. After constructing six constraint equations through two subdomains and four boundary conditions instead of selecting admissible wavefunction bases, a linear algebraic equation was obtained. Then, unknown coefficients of boundary densities were determined by solving the linear algebraic equation. To test the validity of the null-field BIEM, the hybrid method was also used to provide numerical results for comparisons. Only few collocation points on the real boundary and interface are required in the null-field BIEM, so that good results can be obtained. Thanks to the semi-analytical formulation, the null-field BEIM can fully capture the property of geometry and the error only occur from the truncation of the number of the eigenfunction expansion terms in the real implementation. Besides, focusing effect was also observed in the case of a semi-elliptical hill. For the scattering problems of *SH* wave by successive semi-elliptical (circular) hills or canyons, our null-filed BIEM can be straightforward applied to solve those problems.

ACKNOWLEDGMENTS

Financial support from the National Science Council under Grant No. NSC97-2221-E-019-015-MY3 for National Taiwan Ocean University and NTOU No. NTOU-RD-AA-2010-104021 for NTOU/MSV Lab are gratefully acknowledged.

REFERENCES

Abramowitz M. & Stegun I.A., 1965. *Handbook of Mathematical Functions with Formulas, Graphs and Mathematical Tables*, Dover, New York, NY.

Álvarez-Rubio, S., Sánchez-Sesma, F.J., Benito, J.J. & Alarcón, E., 2004. The direct boundary element method: 2D site effects assessment on laterally varying layered media (methodology), *Soil Dyn. Earthq. Eng.,* **24,** 167–180.

Atkinson, K.E., 1997. *The Numerical Solution of Integral Equations of Second Kind,* Cambridge University Press, Cambridge.

Cao, X.R., Song, T.S. & Liu, D.K., 2001. Scattering of plane SH-wave by a cylindrical hill of arbitrary shape, *Appl. Math. Appl. Math. Mech.*, **22**(9), 1082–1089.

Chen, J.T. & Lee, J.W., 2011. Water wave problems using null-field boundary integral equations: ill-posedness and remedies, *Appl. Anal.,* in press.

Chen, J.T. & Wu, A.C., 2007. Null-field approach for the multi-inclusion problem under antiplane shears, *J. appl. Mech.,* **74,** 469–487.

Chen, J.T., Chen, C.T., Chen, P.Y. & Chen, I.L., 2007. A semi-analytical approach for radiation and scattering problems with circular boundaries, *Comput. Methods Appl. Mech. Eng.,* **196,** 2751–2764.

Chen, J.T., Chen, P.Y. & Chen, C.T., 2008a. Surface motion of multiple alluvial valleys for incident plane SH-waves by using a semi-analytical approach, *Soil Dyn. Earthq. Eng.,* **28,** 58–72.

Chen, J.T., Hsiao, C.C. & Leu, S.Y., 2008b. A new method for Stokes problems with circular boundaries using degenerate kernel and Fourier series, *Int. J. numer. Methods Eng.,* **74,** 1955–1987.

Chen, J.T., Lee, Y.T. & Lee, J.W., 2010. Torsional rigidity of an elliptic bar with multiple elliptic inclusions using the null-field integral approach, *Comput. Mech.,* **46,** 511–519.

Chen, J.T., Lee, J.W. & Leu, S.Y., 2011a. Analytical investigation for spurious eigensolutions of multiply-connected membranes containing elliptical boundaries using the dual BIEM, *Int. J. Solids Struct.,* **48,** 729–744.

Chen, J.T., Lee, J.W., Wu, C.F. & Chen, I.L., 2011b. SH-wave diffraction by a semi-circular hill revisited: a null-field boundary integral equation method using degenerate kernels, *Soil Dyn. Earthq. Eng.,* **31,** 729–736.

Cochran, J.A., 1982. *Applied mathematic: Principles, Techniques and Applications,* Wadsworth Publishing, Belmont, CA.

Davis, P.M., Rubinstein, J.L., Liu, K.H., Gao, S.S. & Knopoff, L., 2000. Northridge earthquake damage caused by geologic focusing of seismic waves, *Science,* **289,** 1746–1750.

Fu, L.Y., 2005. Rough surface scattering: comparison of various approximation theories for 2D SH waves, *Bull. seism. Soc. Am.,* **95,** 646–663.

Kamalian, M., Jafari, M.K., Sohrabi-Bidar, A. & Razmkhah, A., 2008. Seismic response of 2-D semi-sine shaped hills to vertically propagating incident waves: amplification patterns and engineering applications, *Earthq. Spectra,* **24**(2), 405–430.

Kawakami, H. & Mogi, H., 2007. Analysis of scattered waves on ground with irregular topography using the direct boundary element and Neumann series expansion, *Bull. seism. Soc. Am.,* **97**(4), 1144–1157.

Kawase, H., 1988. Time-domain response of a semi-circular canyon for incident SV, P and Rayleigh waves calculated by the discrete wavenumber boundary element method, *Bull. seism. Soc. Am.,* **78**(4), 1415–1437.

Komatitsch, D., Liu, Q., Tromp, J., Süss, P., Stidham, C. & Shaw, J.H., 2004. Simulations of ground motion in the Los Angeles basin based upon the spectral-element method, *Bull. seism. Soc. Am.,* **94,** 187–206.

Lee, J.J., 1971. Wave-induced oscillation in harbors of arbitrary geometry, *J. Fluid Mech.,* **45,** 375–394.

Lee, J.W. & Chen, J.T., 2010a. Null-field boundary integral equation approach for hydrodynamic scattering by multiple circular and elliptical cylinders, in *Proceedings of the 8th Asian Computational Fluid Dynamics Conference,* Hong Kong, 2010 January 10–14.

Lee, W.M. & Chen, J.T., 2010b. Scattering of flexural wave in a thin plate with multiple circular inclusions by using the null-field integral equation approach, *J. Sound Vib.,* **329,** 1042–1061.

Lee, V.W., Luo, H. & Liang, J.W., 2006. Antiplane (SH) waves diffraction by a semicircular cylindrical hill revisited: An improved analytical wave series solution, *ASCE J. Eng. Mech.,* **132**(2), 1106–1114.

Mei, C.C., 1980. Boundary layer and finite element techniques applied to wave problem, in *Acoustic, Electromagnetic and Elastic Wave Scattering-Focus on the T-Matrix Approach,* pp. 509–525, eds Varadan, V.V., & Vardan, V.K., Pergamon, New York, NY.

Morse P. & Feshbach H., 1953. *Method of Theoretical Physics,* McGraw-Hill, New York, NY.

Sánchez-Sesma, F.J. & Campillo, M., 1991. Diffraction of P, SV, and Rayleigh waves by topographic features: a boundary integral formulation, *Bull. seism. Soc. Am.,* **81**(6), 2234–2253.

Sánchez-Sesma, F.J., Herrera, I. & Avilés, J., 1982. A boundary method for elastic wave diffraction: application to scattering of SH waves by surface irregularities, *Bull. seism. Soc. Am.,* **72**(2), 473–490.

Sánchez-Sesma, F.J., Vai, R. & Dretta, E., 2001. The variational indirect boundary element method: A strategy toward the solution of very large problems of site response, *J. Comput. Acoust.,* **9**(2), 531–541.

Tompson, J.F., Warsi, Z.U.A. & Mastin, C.W., 1985. *Numerical Grid Generation: Foundations and Applications,* Elsevier Science Publishing Co, New York, NY.

Trifunac, M.D., 1971. Surface motion of a semi-cylindrical alluvial valley for incident plane SH waves, *Bull. seism. Soc. Am.,* **61**(6), 1755–1770.

Trifunac, M.D., 1973. Scattering of plane SH waves by a semi-cylindrical canyon, *Earthq. Eng. Struct. Dyn.,* **1,** 267–281.

Tsaur, D.H. & Chang, K.H., 2009. Scattering and focusing of SH waves by a convex circular-arc topography, *Geophys. J. Int.,* **177,** 222–234.

USGS (U.S. Geological Survey) & SCEC (Southern California Earthquake Center), 1994. The magnitude 6.7 Northridge, California, Earthquake of 17 January 1994, *Science,* **266**(5184), 389–397.

Vogt, R.F., Wolf, J.P. & Bachmann, H., 1988. Wave scattering by a canyon of arbitrary shape in a layered half-space, *Earthq. Eng. Struct. Dyn.,* **16,** 803–812.

Wong, H.L., 1982. Effect of surface topography on the diffraction of *P, SV*, and Rayleigh waves, *Bull. seism. Soc. Am.,* **72,** 1167–1183.

Wong, H.L. & Trifunac, M.D., 1974a. Scattering of plane SH waves by a semi-elliptical canyon, *Earthq. Eng. Struct. Dyn.,* **3,** 157–169.

Wong, H.L. & Trifunac, M.D., 1974b. Surface motion of a semi-elliptical alluvial valley for incident plane *SH* waves, *Bull. seism. Soc. Am.,* **64,** 1389–1408.

Wood, W.D., Jr. & Wood, A.W., 1999. Development and numerical solution of integral equations for electromagnetic scattering from a trough in ground plane, *IEEE Trans Antennas Propag.,* **47**(8), 1388–1322.

Yeh, C.S., Teng, T.J., Shyu, W.S. & Liao, W.I., 2000a. A hybrid method to solve the half-plane radiation problem-numerical verification, in *Proceedings of the 2000 ASME Pressure Vessels and Piping Conference*, Seattle, WA.

Yeh, C.S., Teng, T.J., Shyu, W.S. & Liao, W.I., 2000b. A hybrid method for wave diffraction by a semi-cylindrical alluvial valley, in *Proceedings of the First International Conference on Structural Stability and Dynamics,* Taipei, Taiwan, 2000 December 7–9, pp. 189–198.

Yeh, C.S., Teng, T.J., Shyu, W.S. & Tsai, I.C., 2002. A hybrid method for analyzing the dynamic responses of cavities or shells buried in an elastic half-plane, *The Chin. J. Mech. – Ser. A,* **18**(2), 75–87.

Yeh, C.S., Shyu, W.S., Teng, T.J. & Liao, W.I., 2007. SH wave scattering at a semi-elliptical canyon by hybrid method, in *Proceedings of the 20th KKCNN Symposium on Civil Engineering,* Jeju, Korea, 2007 October 4–5, pp. 25–30.

Yuan, X. & Liao, Z.P., 1994. Scattering of plane SH waves by a cylindrical canyon of circular-arc cross-section, *Soil Dyn. Earthq. Eng.,* **13,** 407–412.

Yuan, X. & Liao, Z.P., 1996. Surface motion of a cylindrical hill of circular-arc cross-section for incident plane SH waves, *Soil Dyn. Earthq. Eng.,* **15,** 189–199.

Yuan, X. & Men, F.L., 1992. Scattering of plane SH waves by a semi-cylindrical hill, *Earthq. Eng. Struct. Dyn.,* **21,** 1091–1098.

Zhang S. & Jin J., 1996. *Computation of Special Functions,* John Wiley & Sons, New York, NY.